Recrystallization and chemical changes in apatite in response to hypervelocity impact

Gavin G. Kenny[1]*, Andreas Karlsson[1], Martin Schmieder[2,3], Martin J. Whitehouse[1], Alexander A. Nemchin[1,4], Jeremy J. Bellucci[1]

[1]*Department of Geosciences, Swedish Museum of Natural History, SE-104 05 Stockholm, Sweden*

[2]*Lunar and Planetary Institute – USRA, 3600 Bay Area Boulevard, Houston TX 77058, USA*

[3]*NASA – Solar System Exploration Research Virtual Institute (SSERVI)*

[4]*School of Earth and Planetary Sciences (EPS), Curtin University, Perth, WA 6845, Australia*

*gkennyeire@gmail.com

SUPPLEMENTARY APPENDIX

Contents

FULL ANALYTICAL METHODS

Apatite, monazite and zircon grains were separated from a sample of clast-rich impact melt rock from Paasselkä by crushing the rock in a jaw crusher and milling the resulting chips in a ring-and-puck-style mill. The heavy minerals were concentrated by magnetic separation with a hand magnet and Frantz magnetic separator, and heavy liquid density separation using methylene iodide diluted to a density of approximately 3.1 g/cm^3. The grains were picked and placed on conductive carbon tabs. These were coated in carbon and the exteriors of the grains were imaged in backscattered electron (BSE) mode on an FEI Quanta FEG 650 scanning electron microscope (SEM) at the Swedish Museum of Natural History, Stockholm. The instrument was operated with an electron beam accelerating voltage of 20 kV and a working distance of 10 mm. The grains were subsequently mounted in 2.5 cm-diameter epoxy mounts and polished with a diamond suspension to expose their interiors. A final polish with colloidal silica prepared the grains for microstructural analysis. The interiors of the grains were imaged in BSE and secondary electron (SE) mode on the SEM described above. Zircon grains were also imaged in cathodoluminescence (CL) mode with a Gatan ChromaCL2 system attached to the SEM.

The chemical compositions of the apatite grains and their inclusions were determined using the FEI Quanta FEG 650 SEM described above. The SEM is fitted with an 80mm^2 X-Max^N Oxford Instruments energy-dispersive X-ray (EDS) detector. Beam current was calibrated against Co-metal, which in turn was calibrated against metal and mineral standards. The apatite was analysed with an operating voltage of 20 kV, beam size of ~2.6 nm, and a working distance of 10 mm. All apatite analyses were conducted in a single session in which analyses repeated a pattern of three to four spots on Durango standard apatite, followed by three to four spots targeting the relict core domain of grain Paass-103ap, in turn followed by three to four spots on neoblasts in the recrystallized region of the grain (Fig. DR1). Due to the minute size of the of $(Mg,Fe)_2(PO_4)F$ inclusions, these were analysed with an operating voltage of 10 kV and a beam size of ~1 nm. This reduced the interaction volume of the electron beam. The instrument was recalibrated against Co-metal in order to accommodate the change in beam current. The full chemical data as shown in Tables DR1-4.

It is important to note that measuring F abundance in apatite by EDS and electron probe microanalysis (EPMA) has well-documented issues (e.g., McCubbin et al., 2011; Goldoff et al., 2012; Ketcham, 2015; and summarised by Webster and Piccolli, 2015). The primary problem for EDS analysis is that it is difficult to confidently separate the line on which F is measured (F-K , 0.677 keV) from a nearby Fe line (Fe-L , 0.705 keV). Although it is difficult to ascertain whether a measured F abundance has been affected by overlapping Fe, Fe itself can be confidently measured as this is done on a separate, interference-free peak (Fe-K , 6.405 keV). In addition to Fe, Mg can also be confidently measured in apatite by EDS as it is measured on the Mg-K peak (1.254 keV).

Electron backscatter diffraction (EBSD) analysis was performed with an Oxford Instruments Nordlys detector attached to the FEI Quanta FEG 650 SEM. The settings and protocols largely

followed established routines for this detector and processing software (Table DR3) (e.g., Timms et al., 2017, and references therein). Well-established match units were used for the analysis of monazite and zircon (Table DR5) (e.g., Erickson et al., 2015; Timms et al., 2017, and references therein). Given the lack of a single match unit for apatite, a range of match units were made in the Twist module of Oxford Instruments' HKL Channel 5 software and used on the apatite grains from Paasselkä. Data for a range of fluorapatite compositions listed in the American Mineralogist crystal structure database (AMCSD) came from Hughes et al. (1989, 1990, 1991, 2004), Fleet and Pan (1995), Rakovan and Hughes (2000), Comodi et al. (2001), McCubbin et al. (2008) and Luo et al. (2009). Two match units were found to index best (see details in Table DR6). Apatite is generally considered to have the space group $P6_3/m$ (number 176 of 230) but all hexagonal space groups (numbers 168-194) were tested here. For the Paasselkä apatite grains and the selected chemical compositions in the match units, the $P6_3$ space group (number 173 of 230) resulted in the best indexing.

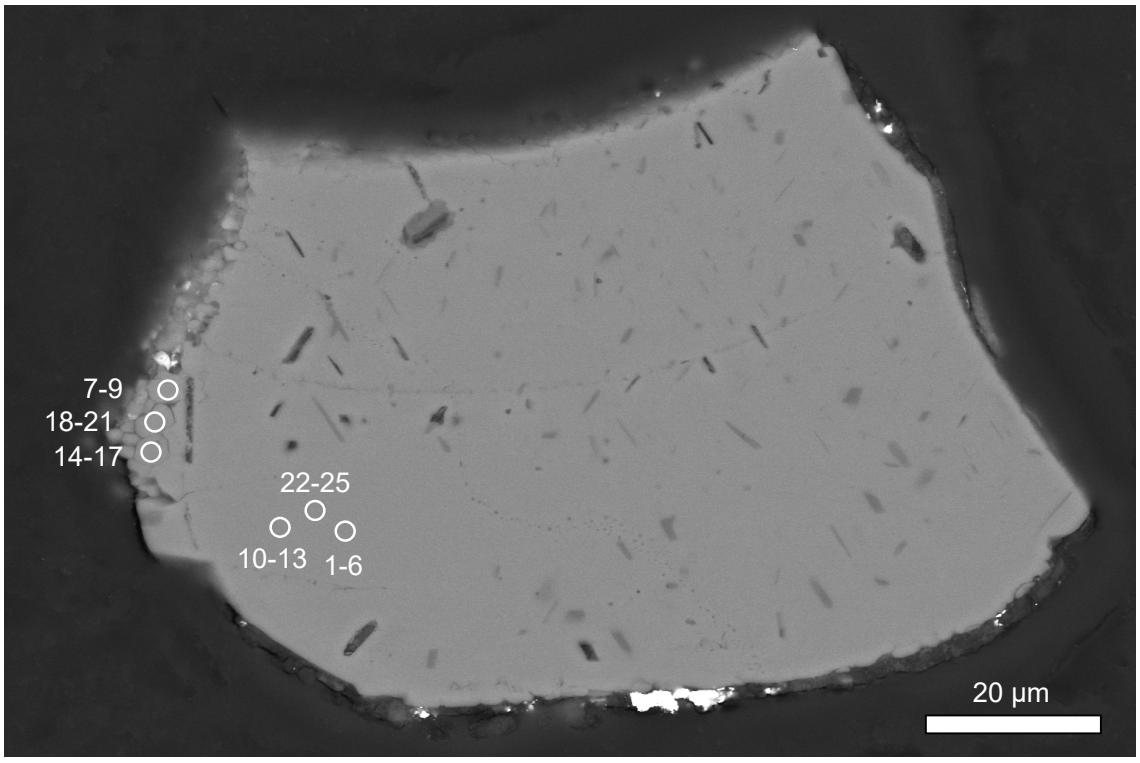

Figure DR1. Backscatter electron image of heterogeneously shock-recrystallized apatite grain Paass-103ap showing locations of energy-dispersive X-ray (EDS) analysis. Data for spots in the relict core domain are shown in Table DR1 and data for spots in neoblasts in the recrystallized domain are shown in Table DR2. These neoblasts were chosen because their outlines are clearly visible so analyses could be confidently conducted within individual neoblasts. Note that the actual areas analyzed are much smaller than the white circle showing location.

Apatite – relict core in Paass-103ap

20 kV, aperture 3 (50 µm)

	Spot #														
Element	**1**	**2**	**3**	**4**	**5**	**6**	**10**	**11**	**12**	**13**	**22**	**23**	**24**	**25**	**average**
F	3.7	3.94	3.58	3.58	3.93	3.96	3.29	3.91	3.54	3.84	3.6	3.59	3.73	4.04	3.73
MgO	1.03	1.05	1.04	1.04	1.03	1.08	1.06	1.11	1.05	1.05	1.06	1.17	1.12	1.07	1.07
P_2O_5	42.31	42.18	42.36	42.36	42.34	42.23	42.7	42.87	42.77	42.86	42.35	42.47	42.35	42.18	42.45
CaO	52.9	52.55	52.92	52.92	52.79	52.86	53.62	53.75	53.48	53.69	52.94	52.8	52.99	52.94	53.08
MnO	0.18	0.16	0.17	0.17	0.17	0.17	0.17	0.16	0.18	0.16	0.19	0.17	0.2	0.16	0.17
FeO	1.07	1.09	1.03	1.03	1.1	1.05	1.01	1.15	1.05	1.08	1.05	1.08	1.02	1.09	1.06
Sum	101.19	100.97	101.1	101.1	101.36	101.35	101.85	102.95	102.07	102.68	101.19	101.28	101.41	101.48	101.57
O = F	-1.56	-1.66	-1.51	-1.51	-1.65	-1.67	-1.39	-1.65	-1.49	-1.62	-1.52	-1.51	-1.57	-1.70	
Total	99.63	99.31	99.59	99.59	99.71	99.68	100.46	101.30	100.58	101.06	99.67	99.77	99.84	99.78	

Normalised to 8 Cations

	Spot #														
APFU	**1**	**2**	**3**	**4**	**5**	**6**	**7**	**8**	**9**	**10**	**11**	**12**	**13**	**14**	**average**
F	0.98	1.05	0.95	0.95	1.05	1.05	0.87	1.02	0.93	1.01	0.96	0.95	0.99	1.08	0.99
Mg	0.13	0.13	0.13	0.13	0.13	0.14	0.13	0.14	0.13	0.13	0.13	0.15	0.14	0.13	0.13
P	3.01	3.02	3.02	3.02	3.02	3.01	3.01	3.00	3.01	3.01	3.01	3.02	3.01	3.00	3.01
Ca	4.77	4.76	4.77	4.77	4.76	4.77	4.78	4.77	4.77	4.77	4.77	4.75	4.77	4.77	4.77
Mn	0.01	0.01	0.01	0.01	0.01	0.01	0.01	0.01	0.01	0.01	0.01	0.01	0.01	0.01	0.01
Fe	0.08	0.08	0.07	0.07	0.08	0.07	0.07	0.08	0.07	0.07	0.07	0.08	0.07	0.08	0.07
Sum cations	8.00	8.00	8.00	8.00	8.00	8.00	8.00	8.00	8.00	8.00	8.00	8.00	8.00	8.00	

Table DR1. Chemical composition of relict core in heterogeneously shock-recrystallized apatite grain Paass-103ap determined by energy-dispersive X-ray analysis. APFU – atoms per formula unit.

Apatite – neoblasts in recrystallized domain in Paass-103ap

20 kV, aperture 3 (50 µm)

	Spot #											
Element	**7**	**8**	**9**	**14**	**15**	**16**	**17**	**18**	**19**	**20**	**21**	**average**
F	3.25	3.12	3.43	3.21	3.13	3.12	3.15	3.65	3.25	3.7	3.46	3.32
MgO	0.34	0.35	0.31	0.31	0.38	0.34	0.34	0.37	0.27	0.32	0.26	0.33
P_2O_5	41.2	41.49	41.23	40.53	41	40.95	40.87	41.58	41.68	41.56	41.64	41.25
CaO	53.12	53.65	53.51	52.46	52.67	52.8	53.06	53	53.38	53.06	53.5	53.11
MnO	0.21	0.17	0.2	0.18	0.21	0.24	0.2	0.24	*b.d.l.*	0.19	0.24	0.21
FeO	0.76	0.7	0.74	0.72	0.71	0.61	0.76	0.79	0.65	0.75	0.73	0.72
Sum	98.88	99.48	99.42	97.41	98.1	98.06	98.38	99.63	99.23	99.58	99.83	98.91
O = F	-1.37	-1.31	-1.44	-1.35	-1.32	-1.31	-1.33	-1.54	-1.37	-1.56	-1.46	
Total	97.51	98.17	97.98	96.06	96.78	96.75	97.05	98.09	97.86	98.02	98.37	

Normalised to 8 Cations

	Spot #											
APFU	**15**	**16**	**17**	**18**	**19**	**20**	**21**	**22**	**23**	**24**	**25**	**average**
F	0.88	0.84	0.93	0.89	0.86	0.85	0.86	0.99	0.88	1.00	0.93	0.90
Mg	0.04	0.04	0.04	0.04	0.05	0.04	0.04	0.05	0.03	0.04	0.03	0.04
P	3.00	2.99	2.99	2.99	3.00	3.00	2.98	3.01	3.02	3.02	3.01	3.00
Ca	4.89	4.90	4.91	4.90	4.88	4.89	4.90	4.86	4.90	4.87	4.89	4.89
Mn	0.02	0.01	0.01	0.01	0.02	0.02	0.01	0.02	*b.d.l.*	0.01	0.02	0.01
Fe	0.05	0.05	0.05	0.05	0.05	0.04	0.05	0.06	0.05	0.05	0.05	0.05
Sum cations	8.00	8.00	8.00	8.00	8.00	8.00	8.00	8.00	8.00	8.00	8.00	

Table DR2. Chemical composition of neoblasts in heterogeneously shock-recrystallized apatite grain Paass-103ap determined by energy-dispersive X-ray analysis. *b.d.l.* – below detection limit. APFU – atoms per formula unit.

Apatite – Durango standard

20 kV, aperture 3 (50 µm)

	Spot #																
Element	**1**	**2**	**3**	**4**	**5**	**6**	**7**	**8**	**9**	**10**	**11**	**12**	**13**	**14**	**15**	**average**	**Lit***
F	3.32	3.19	3.26	3.34	3.36	3.31	3.41	3.3	3.41	3.24	3.51	3.35	3.51	3.3	3.37	3.35	3.35
Na_2O	0.31	0.33	0.28	0.23	0.24	0.24	0.24	0.27	0.26	0.26	0.34	0.18	0.27	0.28	0.25	0.27	0.25
SiO_2	0.49	0.52	0.57	0.59	0.63	0.58	0.55	0.65	0.65	0.54	0.55	0.54	0.56	0.55	0.59	0.57	0.26
P_2O_5	41.1	41.24	41.12	40.91	40.67	40.78	40.34	40.79	40.64	41.08	40.57	40.72	40.17	40.61	40.29	40.74	41.28
SO_3	*b.d.l.*	*b.d.l.*	*b.d.l.*	*b.d.l.*	0.55	*b.d.l.*	0.48	0.5	*b.d.l.*	*b.d.l.*	*b.d.l.*	*b.d.l.*	0.48	0.51	0.47	0.50	0.38
Cl	0.38	0.39	0.41	0.43	0.41	0.43	0.42	0.43	0.43	0.43	0.41	0.4	0.43	0.43	0.44	0.42	0.46
CaO	54.51	54.4	54.25	54.55	54.39	54.21	54.02	54	53.83	54.21	54.54	54.18	54.04	54.14	54.04	54.22	54.19
FeO	0.11	0.01	0.06	0.03	0.06	0.03	0.07	0.06	0.1	0.03	0.04	0.04	0.04	0.08	0.02	0.05	0.06
Ce_2O_3	0.5	0.55	0.64	*b.d.l.*	*b.d.l.*	0.74	*b.d.l.*	0.65	*b.d.l.*	0.68	*b.d.l.*	0.47	*b.d.l.*	0.46	0.65	0.59	0.52
Sum	100.72	100.63	100.59	100.08	100.31	100.32	99.53	100.65	99.32	100.47	99.96	99.88	99.5	100.36	100.12	100.16	100.75
O = F	-1.40	-1.34	-1.37	-1.41	-1.41	-1.39	-1.44	-1.39	-1.44	-1.36	-1.48	-1.41	-1.48	-1.39	-1.42		
O = Cl	-0.09	-0.09	-0.09	-0.10	-0.09	-0.10	-0.09	-0.10	-0.10	-0.10	-0.09	-0.09	-0.10	-0.10	-0.10		
Total	99.24	99.20	99.12	98.58	98.80	98.83	98.00	99.16	97.79	99.01	98.39	98.38	97.92	98.87	98.60		

Normalised to 8 Cations

	Spot #															
APFU	**1**	**2**	**3**	**4**	**5**	**6**	**7**	**8**	**9**	**10**	**11**	**12**	**13**	**14**	**15**	**average**
F	0.89	0.85	0.87	0.90	0.90	0.89	0.92	0.89	0.92	0.87	0.94	0.91	0.95	0.89	0.91	0.90
Na	0.05	0.05	0.05	0.04	0.04	0.04	0.04	0.04	0.04	0.04	0.06	0.03	0.04	0.05	0.04	0.04
Si	0.04	0.04	0.05	0.05	0.05	0.05	0.05	0.06	0.06	0.05	0.05	0.05	0.05	0.05	0.05	0.05
P	2.94	2.95	2.95	2.94	2.92	2.94	2.92	2.93	2.95	2.95	2.92	2.95	2.91	2.92	2.91	2.94
S	*b.d.l.*	*b.d.l.*	*b.d.l.*	*b.d.l.*	0.04	*b.d.l.*	0.03	0.03	*b.d.l.*	*b.d.l.*	*b.d.l.*	*b.d.l.*	0.03	0.03	0.03	0.03
Cl	0.05	0.06	0.06	0.06	0.06	0.06	0.06	0.06	0.06	0.06	0.06	0.06	0.06	0.06	0.06	0.06
Ca	4.94	4.93	4.93	4.97	4.95	4.95	4.95	4.91	4.94	4.93	4.97	4.96	4.96	4.93	4.94	4.94
Fe	0.01	0.00	0.00	0.00	0.00	0.00	0.01	0.00	0.01	0.00	0.00	0.00	0.00	0.01	0.00	0.00
Ce	0.02	0.02	0.02	*b.d.l.*	*b.d.l.*	0.02	*b.d.l.*	0.02	*b.d.l.*	0.02	*b.d.l.*	0.01	*b.d.l.*	0.01	0.02	0.02
Sum cations	8.00	8.00	8.00	8.00	8.00	8.00	8.00	8.00	8.00	8.00	8.00	8.00	8.00	8.00	8.00	

Table DR3. Chemical composition of Durango apatite standard determined by energy-dispersive X-ray analysis in the same session as data reported in Tables DR1-2. *Literature value from Marks et al. (2012). *b.d.l.* – below detection limit. APFU – atoms per formula unit.

$(Mg,Fe)_2(PO_4)F$ inclusions

10 kV, aperture 5 (30 µm)

	Spot #					
Element	**1**	**2**	**3**	**4**	**5**	**average**
F	11.22	11.07	11.09	11.03	10.92	11.07
MgO	41.93	40.93	41.67	42.25	41.76	41.71
SiO_2	*b.d.l.*	*b.d.l.*	*b.d.l.*	0.37	*b.d.l.*	0.37
P_2O_5	39.57	39.65	40.08	39.67	39.43	39.68
CaO	0.88	1.52	0.64	0.81	1.17	1.00
FeO	6.38	6.12	5.97	6.67	6.30	6.29
SUM	99.98	99.29	99.44	100.80	99.58	99.82
O = F	-4.72	-4.66	-4.67	-4.65	-4.60	
Total	95.26	94.63	94.77	96.16	94.98	

Normalised to 8 Cations

	Spot #					
APFU	**1**	**2**	**3**	**4**	**5**	**average**
F	1.04	1.04	1.03	1.01	1.01	1.03
Mg	1.83	1.81	1.83	1.83	1.83	1.83
Si	*b.d.l.*	*b.d.l.*	*b.d.l.*	0.01	*b.d.l.*	0.01
P	0.98	0.99	1.00	0.97	0.98	0.99
Ca	0.03	0.05	0.02	0.03	0.04	0.03
Fe	0.16	0.15	0.15	0.16	0.15	0.15
Sum cations	3.00	3.00	3.00	3.00	3.00	

Table DR4. Chemical composition of $(Mg,Fe)_2(PO_4)F$ (wagnerite or a polymorph thereof) inclusions determined by energy-dispersive X-ray analysis. *b.d.l.* – below detection limit. APFU – atoms per formula unit.

SEM	
Make/model	FEI Quanta FEG 650 SEM
Location	Swedish Museum of Natural History, Stockholm
EBSD acquisition system	Oxford Instruments Nordlys detector
EBSD processing software	Oxford Instruments HKL Channel 5.12
Accelerating voltage	20 kV
Working distance	~18 mm
Tilt	70°

EBSD match units	
Apatite	Hughes et al. (1991) (AMCSD: 1377), Fleet and Pan (1995) (AMCSD: 1727)
Monazite	Ni et al. (1995)
Zircon	Hazen and Finger (1979); 1 atm
Reidite	Farnan et al. (2003); 0.69 GPa
Baddeleyite (monoclinic ZrO_2)	Howard et al. (1988)

EBSP acquisition, indexing and processing						
Grain ID	(Paass-)	103ap	106ap	107ap	202z	213m
Figure(s)		4	3, DR2	3, DR3	DR5	DR6
EBSP acquisition speed (Hz)		40	40	40	40	40
EBSP background (frames)		128	128	128	128	128
EBSP binning		1x1	1x1	1x1	2x2	2x2
EBSP gain		High	High	High	High	High
Frame averaging		4	8	8	1	1
Hough resolution		60	60	60	60	60
Band detection (min/max)		6/8	6/8	6/8	6/8	6/8
Map step size (nm)		150	400	300	150	75
X steps		682	205	203	794	1049
Y steps		544	301	211	606	797

EBSD noise reduction routine						
Wildspike correction		Yes	Yes	Yes	Yes	Yes
Kuwahara Filter		No	No	No	No	No
Nearest neighbour zero solution extrapolation		6	6	6	6	6

Table DR5. Scanning electron microscopy settings and electron backscatter diffraction (EBSD) analysis acquisition and processing parameters. EBSP – electron backscatter patterns.

Hughes et al., 1991 (AMCSD: 1377)					**Fleet and Pan, 1995 (AMCSD: 1727)**				
Space group	$P6_3$ (number 173)*				**Space group**	$P6_3$ (number 173)*			
a (Å)	9.4052				**a (Å)**	9.4123			
b (Å)	9.4052				**b (Å)**	9.4123			
c (Å)	6.9125				**c (Å)**	6.9080			
α (°)	90				**α (°)**	90			
β (°)	90				**β (°)**	90			
γ (°)	120				**γ (°)**	120			
Wyckoff positions	**x**	**y**	**z**	**occ.**	**Wyckoff positions**	**x**	**y**	**z**	**occ.**
Ca1	2/3	1/3	-0.0012	0.677	**Ca1**	2/3	1/3	0.0006	0.888
Na1	2/3	1/3	-0.0012	0.237	**Na1**	2/3	1/3	0.0006	0.089
Ce1	2/3	1/3	-0.0012	0.086	**La1**	2/3	1/3	0.0006	0.023
Ca2	0.98860	0.23885	0.25	0.847	**Ca2**	0.98989	0.24018	0.25	0.907
Ce2	0.98860	0.23885	0.25	0.153	**La2**	0.98989	0.24018	0.25	0.093
P	0.36881	0.39692	0.25	0.947	**P**	0.36898	0.39808	0.25	0.952
Si	0.36881	0.39692	0.25	0.053	**Si**	0.36898	0.39808	0.25	0.048
O1	0.4821	0.3233	0.25		**O1**	0.4847	0.3268	0.25	
O2	0.4671	0.5853	0.25		**O2**	0.4663	0.5872	0.25	
O3	0.2557	0.3396	0.0721		**O3**	0.2568	0.3406	0.0716	
F	0	0	0.25		**F**	0	0	0.25	

Table DR6. Match units for apatite used in this study. Data from Hughes et al. (1991) and Fleet and Pan (1995). *note that the space group used in this study, $P6_3$ (number 173), is not that quoted in the American Mineralogist crystal structure database (AMCSD), $P6_3/m$ (number 176).

REFERENCES CITED

Comodi, P., Liu, Y., Zanazzi, P. F., and Montagnoli, M., 2001, Structural and vibrational behaviour of fluorapatite with pressure. Part I: in situ single-crystal X-ray diffraction investigation: Physics and Chemistry of Minerals, v. 28, no. 4, p. 219-224, https://doi.org/10.1007/s002690100154.

Erickson, T. M., Pearce, M. A., Taylor, R. J. M., Timms, N. E., Clark, C., Reddy, S. M., and Buick, I. S., 2015, Deformed monazite yields high-temperature tectonic ages: Geology, v. 43, no. 5, p. 383-386, https://doi.org/10.1130/g36533.1.

Farnan, I., Balan, E., Pickard, C. J., and Mauri, F., 2003, The effect of radiation damage on local structure in the crystalline fraction of $ZrSiO_4$: Investigating the ^{29}Si NMR response to pressure in zircon and reidite: American Mineralogist, v. 88, no. 11-12, p. 1663-1667, https://doi.org/10.2138/am-2003-11-1205.

Fleet, M. E., and Pan, Y., 1995, Site preference of rare earth elements in fluorapatite: American Mineralogist, v. 80, no. 3-4, p. 329-335, https://doi.org/10.2138/am-1995-3-414.

Goldoff, B., Webster, J. D., and Harlov, D. E., 2012, Characterization of fluor-chlorapatites by electron probe microanalysis with a focus on time-dependent intensity variation of halogens: American Mineralogist, v. 97, p. 1103–1115, https://doi.org/10.2138/am.2012.3812.

Hazen, R. M., and Finger, L. W., 1979, Crystal structure and compressibility of zircon at high pressure: American Mineralogist, v. 64, p. 196-201,

Howard, C. J., Hill, R. J., and Reichert, B. E., 1988, Structures of ZrO_2 polymorphs at room temperature by high resolution neutron powder diffraction: Acta Crystallographica Section B, v. 44, no. 2, p. 116-120, https://doi.org/10.1107/S0108768187010279.

Hughes, J. M., Cameron, M., and Crowley, K. D., 1989, Structural variations in natural F, OH, and Cl apatites: American Mineralogist, v. 74, no. 7-8, p. 870-876,

Hughes, J. M., Cameron, M., and Crowley, K. D., 1990, Crystal structures of natural ternary apatites; solid solution in the $Ca_5(PO_4)_3X$ (X = F, OH, Cl) system: American Mineralogist, v. 75, no. 3-4, p. 295-304,

Hughes, J. M., Cameron, M., and Mariano, A. N., 1991, Rare-earth-element ordering and structural variations in natural rare-earth-bearing apatites: American Mineralogist, v. 76, p. 1165-1173,

Hughes, J. M., Ertl, A., Bernhardt, H.-J. r., Rossman, G. R., and Rakovan, J., 2004, Mn-rich fluorapatite from Austria: Crystal structure, chemical analysis, and spectroscopic investigations: American Mineralogist, v. 89, no. 4, p. 629-632, https://doi.org/10.2138/am-2004-0417.

Ketcham, R. A., 2015, Calculation of stoichiometry from EMP data for apatite and other phases with mixing on monovalent anion sites: American Mineralogist, v. 100, no. 7, p. 1620-1623, https://doi.org/10.2138/am-2015-5171.

Luo, Y., Hughes, J. M., Rakovan, J., and Pan, Y., 2009, Site preference of U and Th in Cl, F, and Sr apatites: American Mineralogist, v. 94, no. 2-3, p. 345-351, https://doi.org/10.2138/am.2009.3026.

Marks, M. A. W. et al., 2012, The volatile inventory (F, Cl, Br, S, C) of magmatic apatite: An integrated analytical approach: Chemical Geology, v. 291, p. 241–255, https://doi.org/10.1016/j.chemgeo.2011.10.026.

McCubbin, F. M., Jolliff, B. L., Nekvasil, H., Carpenter, P. K., Zeigler, R. A., Steele, A., Elardo, S. M., and Lindsley, D. H., 2011, Fluorine and chlorine abundances in lunar apatite: Implications for heterogeneous distributions of magmatic volatiles in the lunar interior: Geochimica et Cosmochimica Acta, v. 75, p. 5073–5093, https://doi.org/10.1016/j.gca.2011.06.017.

McCubbin, F. M., Mason, H. E., Park, H., Phillips, B. L., Parise, J. B., Nekvasil, H., and Lindsley, D. H., 2008, Synthesis and characterization of low-OH fluor-chlorapatite: A single-crystal

XRD and NMR spectroscopic study: American Mineralogist, v. 93, no. 1, p. 210-216, https://doi.org/10.2138/am.2008.2557.

Ni, Y., Hughes, J. M., and Mariano, A. N., 1995, Crystal chemistry of the monazite and xenotime structures: American Mineralogist, v. 80, no. 1-2, p. 21-26, https://doi.org/10.2138/am-1995-1-203.

Rakovan, J. F., and Hughes, J. M., 2000, Strontium in the apatite structure: strontian fluorapatite and belovite-(Ce): The Canadian Mineralogist, v. 38, no. 4, p. 839-845, https://doi.org/10.2113/gscanmin.38.4.839.

Timms, N. E., Erickson, T. M., Pearce, M. A., Cavosie, A. J., Schmieder, M., Tohver, E., Reddy, S. M., Zanetti, M. R., Nemchin, A. A., and Wittmann, A., 2017, A pressure-temperature phase diagram for zircon at extreme conditions: Earth-Science Reviews, v. 165, p. 185-202, https://doi.org/10.1016/j.earscirev.2016.12.008.

Webster, J. D., and Piccoli, P. M., 2015, Magmatic apatite: A powerful, yet deceptive, mineral: Elements, v. 11, p. 177–182, https://doi.org/10.2113/gselements.11.3.177.

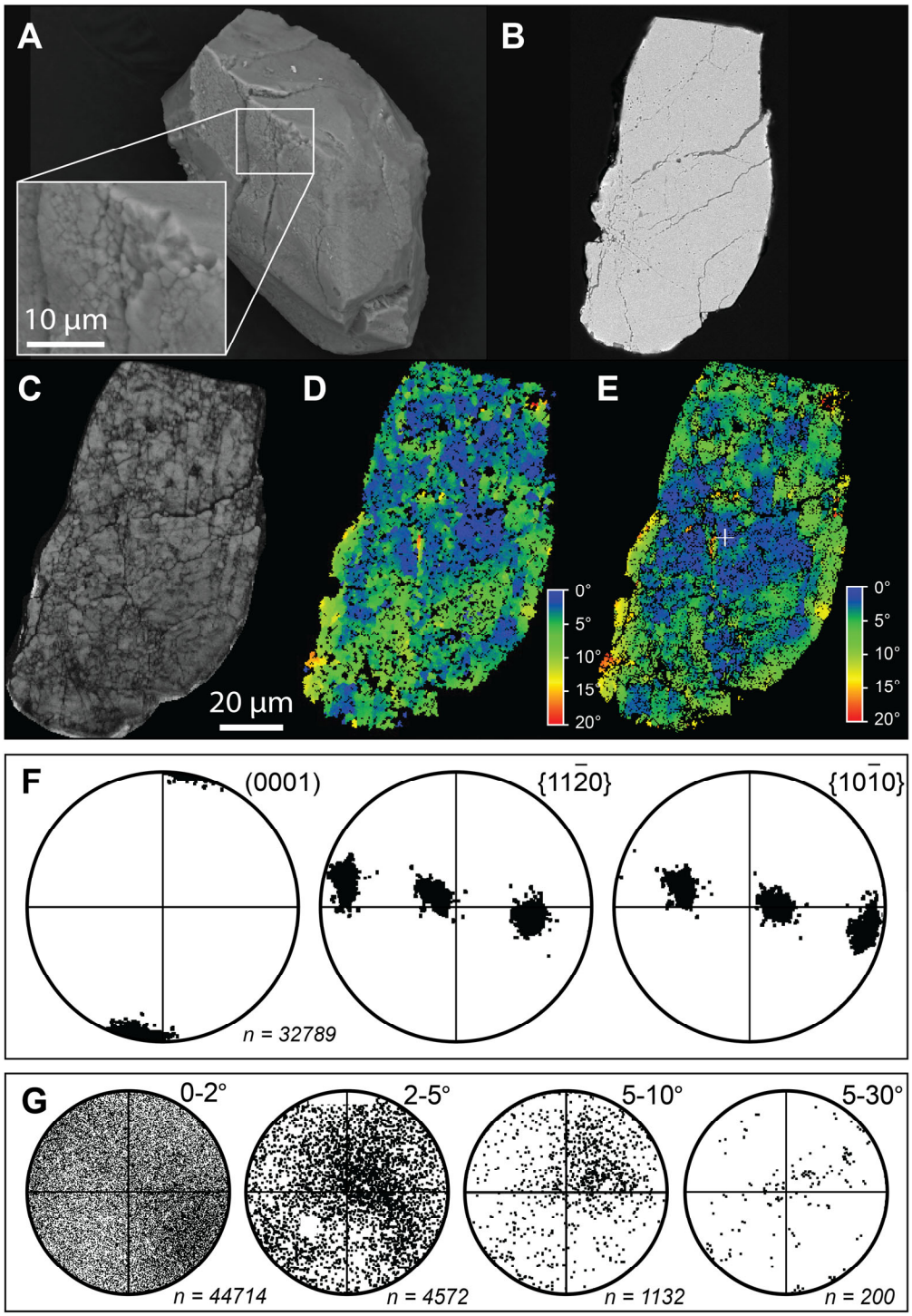

Figure DR2. Shock-recrystallized apatite grain Paass-106ap from the Paasselkä impact structure, Finland. A: Backscattered electron (BSE) image of grain exterior. **B:** BSE image of grain interior. **C:** Electron backscatter diffraction (EBSD) band contrast (BC) image. **D:** Map showing grain reference orientation deviation (GROD) angle (the average orientation is determined for each grain; the deviation angle from this mean orientation is then plotted for each point). **E**: Map showing crystallographic misorientation relative to a reference point (white cross) **F:** Pole figures – equal-area, lower-hemisphere projections. **G:** Misorientation axes binned by misorientation angle and plotted in equal-area projections. Step size = 400 nm.

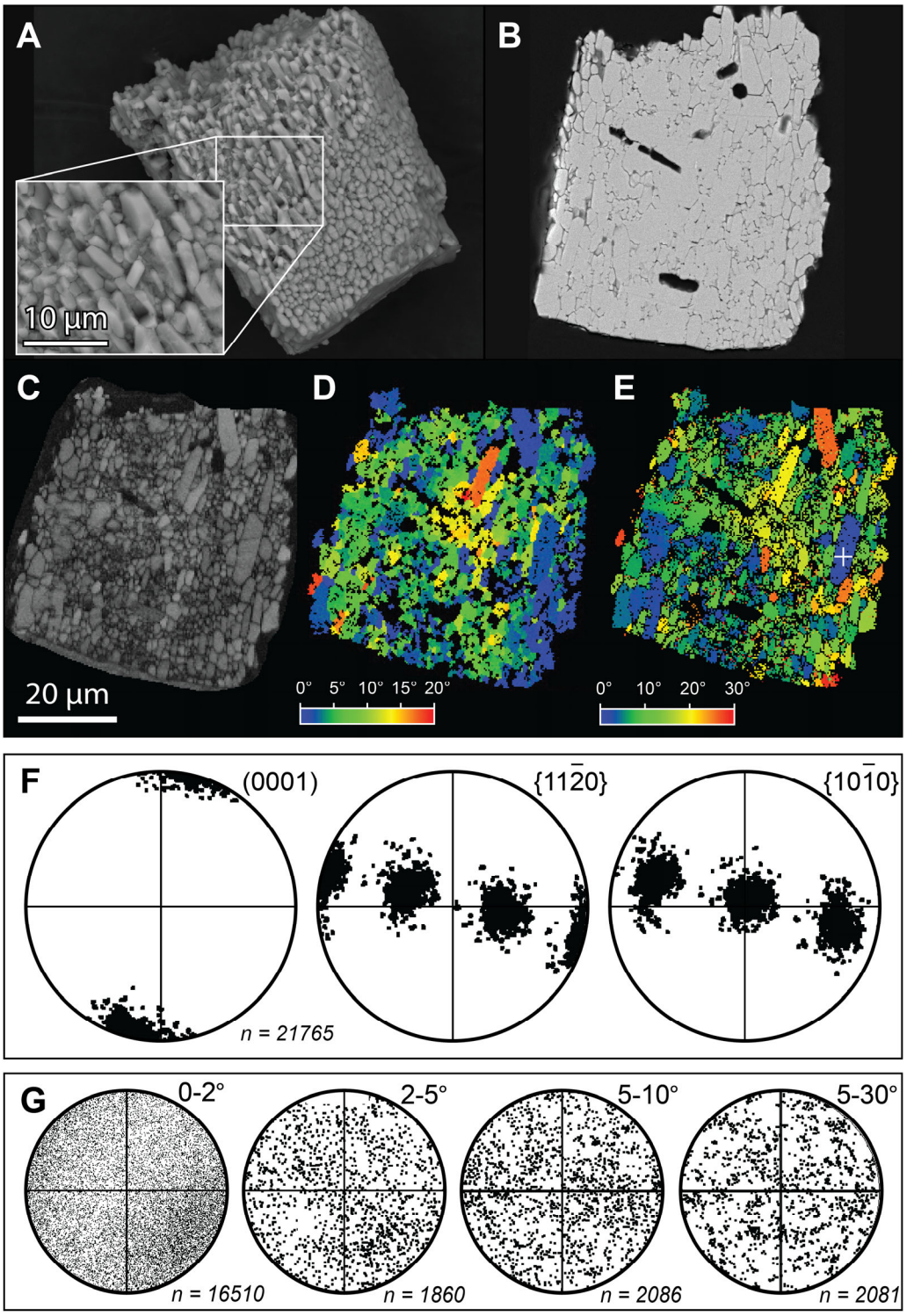

Figure DR3. Shock-recrystallized apatite grain Paass-107ap from the Paasselkä impact structure, Finland. A: Backscattered electron (BSE) image of grain exterior. **B:** BSE image of grain interior. **C:** Electron backscatter diffraction (EBSD) band contrast (BC) image. **D**: Map showing grain reference orientation deviation (GROD) angle (see definition in caption of Fig. DR1). **E:** Map showing crystallographic misorientation relative to a reference point (white cross) **F:** Pole figures – equal-area, lower-hemisphere projections. **G:** Misorientation axes binned by misorientation angle and plotted in equal-area projections. Step size = 300 nm.

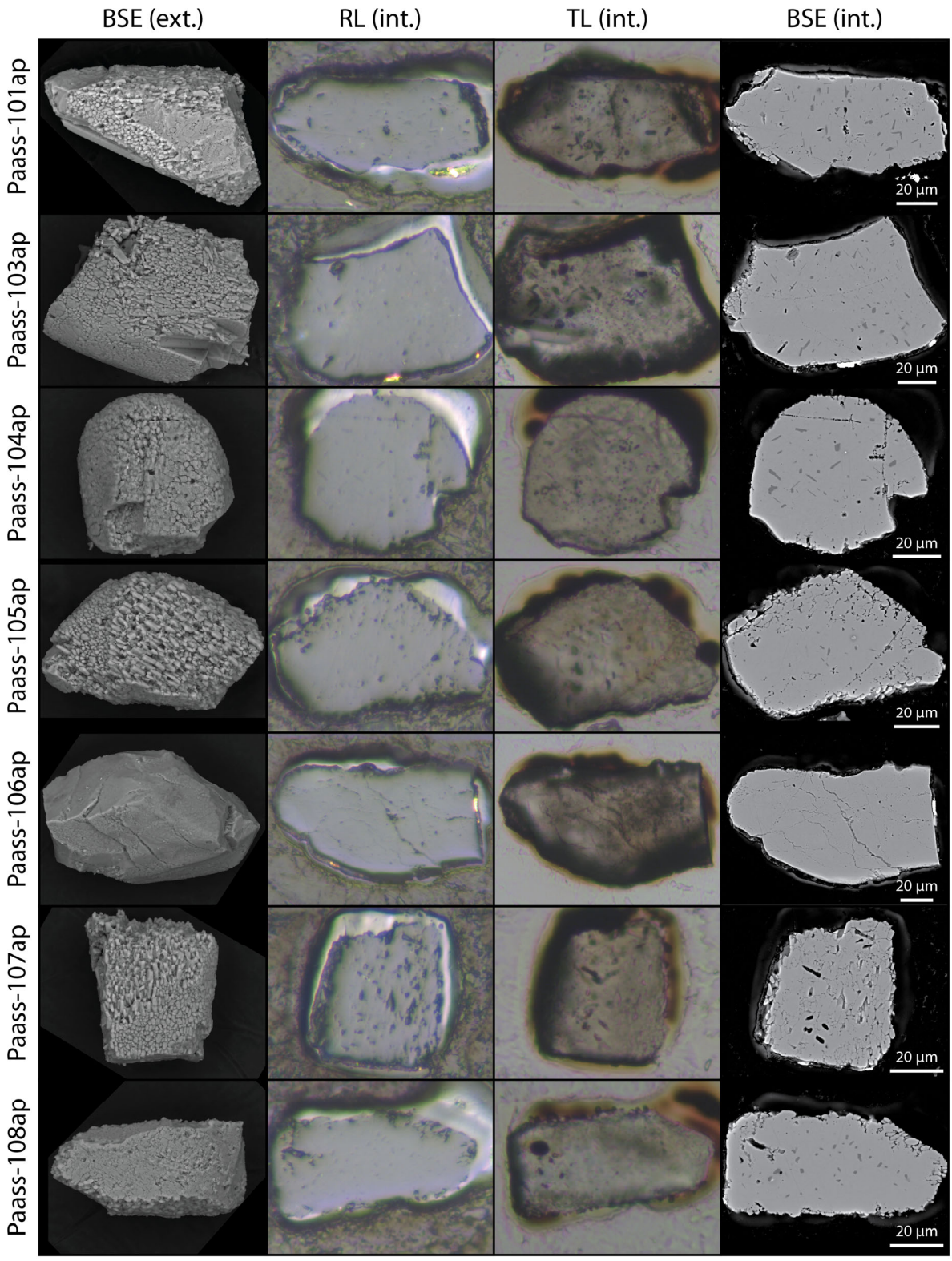

Figure DR4. Images of shocked apatite from Paasselkä. From left to right, columns show backscattered electron (BSE) images of grain exteriors (ext.), reflected light (RL) images of grain interiors (int.), transmitted light (TL) images of grain interiors and BSE images of grain interiors. The black and brown areas around the grains (in TL images) are a result of the electron beam burning the epoxy during the electron backscatter diffraction (EBSD) analyses.

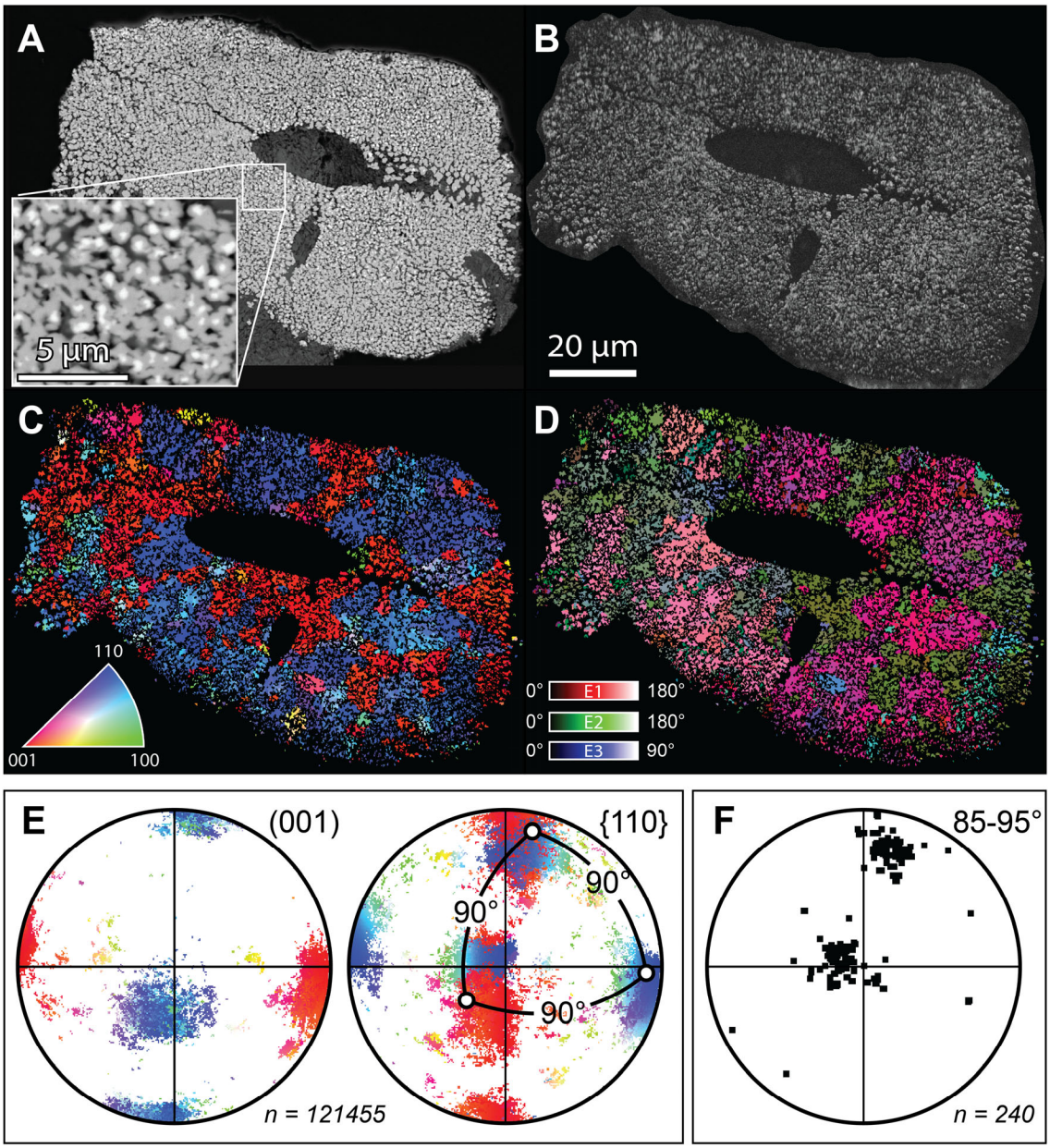

Figure DR5. An example of shock-recrystallized zircon from the Paasselkä impact structure, Finland. A: Backscattered electron (BSE) image. The brighter spots visible in the inset image are ZrO_2 cores in the $ZrSiO_4$ granules. Granular zircon grains in this sample of impact melt rock invariably display ZrO_2-rich cores in effectively all granules. **B:** Electron backscatter diffraction (EBSD) band contrast (BC) image. **C:** Image colored according to the inset inverse pole figure (IPF). Note that the grain is composed of multiple discrete domains of similarly orientated neoblasts. **D:** Crystallographic orientation in Euler coordinate space. **E:** Pole figures colored according to IPF map in C. **F:** Plot showing high-angle (85° to 95°) misorientation axes. The observations of (i) domains of neoblasts systematically misoriented by 90°, (ii) coincidence among (001) and {110} poles, and (iii) high-angle misorientation axes coincident with poles to {110} are consistent with the former presence of reidite in this grain. Stereonets are equal-area, lower-hemisphere projections. Step size = 150 nm.

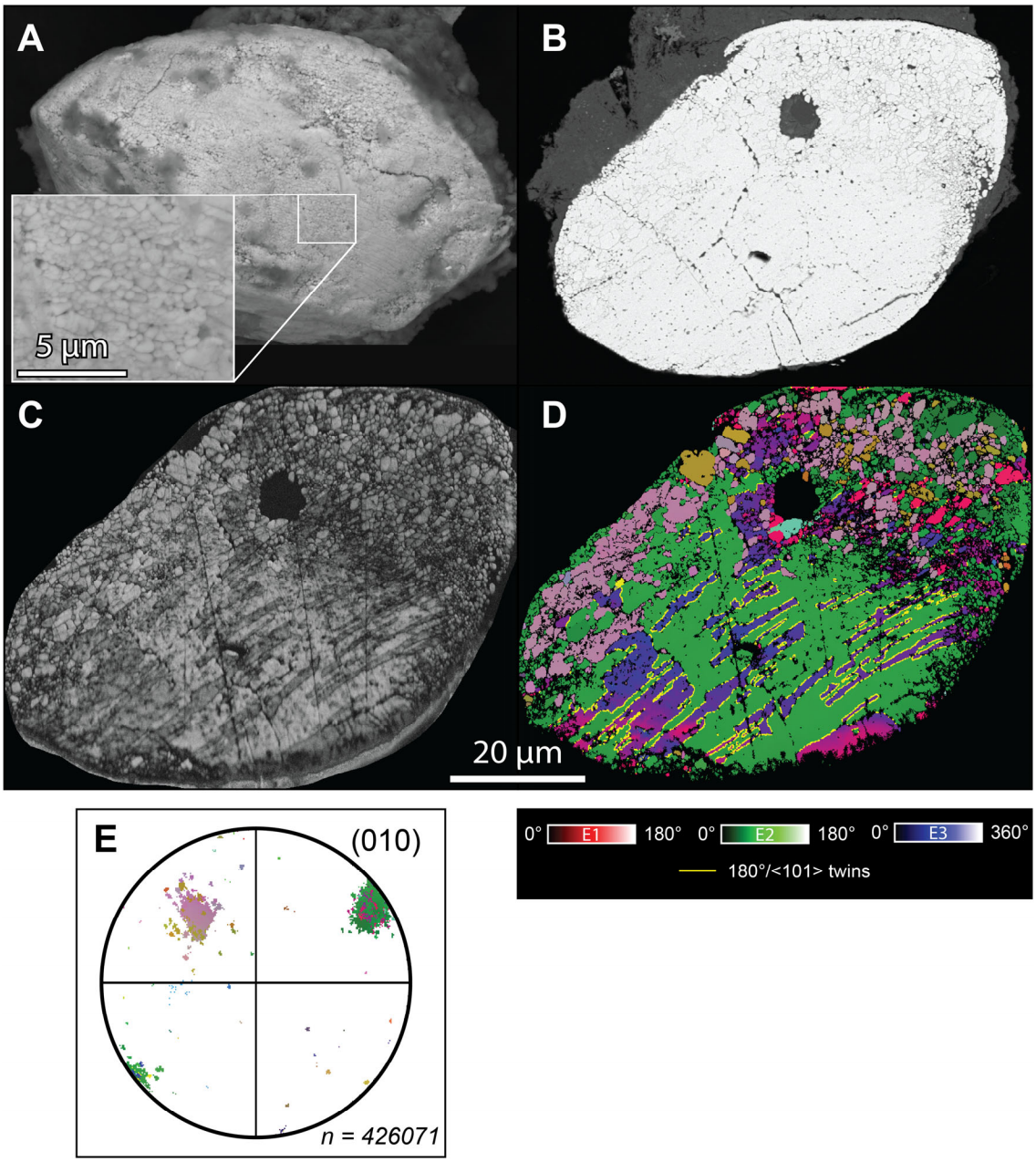

Figure DR6. An example of shock-recrystallized monazite from the Paasselkä impact structure, Finland. A: Backscattered electron (BSE) image of grain exterior with granular texture readily visible in inset. **B:** BSE image of grain interior. **C:** Electron backscatter diffraction (EBSD) band contrast (BC) image. **D:** Map showing crystallographic orientation in Euler coordinate space and 180°/<101> twins in yellow. **E:** Pole figure colored according to the Euler map shown in D. The neoblasts (pink-beige color) are misoriented from the host grain (green color) by approximately 100°. Stereonet is equal-area, lower-hemisphere projection. Step size = 75 nm.